Bioactive Materials 32 (2024) 400–414

Contents lists available at ScienceDirect

Bioactive Materials

journal homepage: www.keaipublishing.com/en/journals/bioactive-materials

# Full-thickness osteochondral defect repair using a biodegradable bilayered scaffold of porous zinc and chondroitin sulfate hydrogel

Fan Yang [a,1], Yageng Li [b,1], Lei Wang [b,1], Haodong Che [b], Xin Zhang [a], Holger Jahr [c,d], Luning Wang [b], Dong Jiang [a,**], Hongjie Huang [a,***], Jianquan Wang [a,*]

[a] Department of Sports Medicine, Peking University Third Hospital, Institute of Sports Medicine of Peking University, Beijing Key Laboratory of Sports Injuries, Engineering Research Center of Sports Trauma Treatment Technology and Devices, Ministry of Education, Beijing, China
[b] Beijing Advanced Innovation Center for Materials Genome Engineering, State Key Laboratory for Advanced Metals and Materials, School of Materials Science and Engineering, University of Science and Technology Beijing, Beijing, China
[c] Institute of Anatomy and Cell Biology, University Hospital RWTH Aachen, Aachen, 52074, Germany
[d] Institute of Structural Mechanics and Lightweight Design, RWTH Aachen University, 52062, Aachen, Germany

ARTICLE INFO

*Keywords:*
Chondroitin sulfate hydrogel
Additive manufacturing
Porous Zn scaffold
Osteochondral regeneration

ABSTRACT

The regeneration of osteochondral tissue necessitates the re-establishment of a gradient owing to the unique characteristics and healing potential of the chondral and osseous phases. As the self-healing capacity of hyaline cartilage is limited, timely mechanical support during neo-cartilage formation is crucial to achieving optimal repair efficacy. In this study, we devised a biodegradable bilayered scaffold, comprising chondroitin sulfate (CS) hydrogel to regenerate chondral tissue and a porous pure zinc (Zn) scaffold for regeneration of the underlying bone as mechanical support for the cartilage layer. The photocured CS hydrogel possessed a compressive strength of 82 kPa, while the porous pure Zn scaffold exhibited a yield strength of 11 MPa and a stiffness of 0.8 GPa. Such mechanical properties are similar to values reported for cancellous bone. In vitro biological experiments demonstrated that the bilayered scaffold displayed favorable cytocompatibility and promoted chondrogenic and osteogenic differentiation of bone marrow stem cells. Upon implantation, the scaffold facilitated the simultaneous regeneration of bone and cartilage tissue in a porcine model, resulting in (i) a smoother cartilage surface, (ii) more hyaline-like cartilage, and (iii) a superior integration into the adjacent host tissue. Our bilayered scaffold exhibits significant potential for clinical application in osteochondral regeneration.

## 1. Introduction

Osteochondral lesions and defects in joints are prevalent and pose a significant health concern, resulting in knee joint pain, dysfunction, and, ultimately, disability [1–3]. These lesions can arise from various causes, including osteoarthritis, osteochondritis dissecans, osteochondral fractures, osteonecrosis, and traumatic injuries [4]. While bone tissue is vascularized and possesses intrinsic regenerative capabilities, cartilage is avascular, aneural, and alymphatic, which limits its capacity for self-repair [5]. The function of cartilage is to mitigate underlying bone pressure by serving as a shock absorber, and its efficacy is contingent upon the mechanical reinforcement provided by subchondral bone. Biochemically, structurally, and mechanically, bone and cartilage are dissimilar [6,7]. Consequently, the disparate properties of osseous and chondral tissues and their distinct healing capacities render the treatment of an osteochondral defect challenging [8].

Traditional clinical therapeutic approaches, such as microfracture, osteochondral grafts, and autologous cell transplantation, do not successfully improve the structure and function of the affected areas [9–11]. Tissue engineering, which involves creating a scaffold that mimics tissue, offers a flexible solution for osteochondral regeneration [12]. It is necessary to rehabilitate both the cartilage and its subchondral

Peer review under responsibility of KeAi Communications Co., Ltd.
* Corresponding author.
** Corresponding author.
*** Corresponding author.
*E-mail addresses:* bysyjiangdong@126.com (D. Jiang), bysyhhj@163.com (H. Huang), wjqsportsmed@163.com (J. Wang).
[1] These authors contributed equally: F.Yang, Y.Li, and L.Wang.

https://doi.org/10.1016/j.bioactmat.2023.10.014
Received 25 August 2023; Received in revised form 26 September 2023; Accepted 15 October 2023

bone simultaneously to treat an osteochondral lesion, as early mechanical support during neo-cartilage formation is crucial for achieving optimal repair efficacy [13]. The cartilaginous component necessitates a hydrated viscoelastic matrix with a relatively low compressive modulus, while the osseous component requires a rigid framework with a relatively high modulus [14]. The mechanical properties of currently reported single-phase scaffolds do not fulfill these requirements. Tissue engineering requires strategies that can better recapitulate the spatial complexity of the native tissue and its interface with the subchondral bone [15]. Bilayer scaffolds were developed with gradient properties and incorporated gradient features to address this issue. The bone layer of the bilayer scaffold strategy was composed of either Ti6Al4V [16,17] or tantalum [18], which exhibited compressive strengths ranging from 43.04 to 73 MPa, significantly higher than that of cancellous bone (up to 15.1 MPa and decreased with age [19]). Furthermore, the elastic modulus of porous Ti6Al4V and titanium was notably higher than that of cancellous bone [20]. Moreover, the presence of non-degraded material may require surgical intervention [11], thereby further constraining the effectiveness of this bilayer scaffold treatment methodology.

Zn is an essential trace element in the human body, playing a crucial role in various fundamental biological processes, such as nucleic acid metabolism, signal transduction, and gene expression. Additionally, Zn enhances the osteogenic differentiation of bone marrow mesenchymal stem cells, with 86% of its mass present in skeletal muscle and bone [21–25]. Furthermore, Zn-based materials exhibit superior biodegradation characteristics compared to Mg-based materials as they do not generate hydrogen gas and do not cause significant pH fluctuations [26]. The excessive degradation rates of Mg-based materials and low degradation rates of iron-based materials in biological environments have restricted their use as bone implants [27–29]. In contrast, Zn-based materials exhibit a more suitable rate of bone regeneration, offering long-lasting mechanical support while fully degrading [23,30]. The utilization of additive manufacturing (AM) has facilitated the precise fabrication of Zn scaffolds with intricate internal structures and personalized external geometries. These AM Zn scaffolds possess significant potential to satisfy the criteria for optimal bone scaffolds, such as mechanical properties that match those of bones, interconnected porous structures, adjustable degradation rates, and favorable biocompatibility [30–34].

The present study aimed to develop a biodegradable bilayer scaffold comprising a porous Zn scaffold for the bone layer and a photocuring chondroitin sulfate (CS) hydrogel scaffold for the cartilage layer (Fig. 1). Photocurable hydrogel precursors were used to enable rapid crosslinking under physiological conditions, thereby avoiding large temperature or pH fluctuations in biological tissue. Additionally, the photocuring process allowed for precise spatial and temporal control of gelation, facilitating application to complex shapes and rendering the hydrogel suitable for in situ injectable cartilage repair [35–38]. CS is a sulfated glycosaminoglycan that exhibits numerous biological effects, including anti-inflammatory properties and promotion of cellular growth. Following chemical modification, CS hydrogel can be synthesized via photocuring. The resultant CS hydrogel demonstrates favorable biocompatibility and biodegradability, rendering it suitable for biomedical applications such as cartilage repair [39,40]. This study examines the in vitro mechanical properties, degradation behavior, biocompatibility, and osteogenic and chondrogenic effects of a bilayer porous Zn-hydrogel scaffold. The efficacy of the scaffold in repairing an osteochondral defect model of the trochlear groove of Bama mini pigs was evaluated in vivo. The study did not utilize exogenously infused chondrogenic cells [7,41] or bioactivity growth factors [42,43]. Instead, the scaffold was designed to recruit the body's stem/progenitor cells to the defect site, thereby obviating the need for pre-implantation cell loading [44]. The bilayer scaffold, comprising biodegradable metal and hydrogel, exhibits significant potential for clinical application in osteochondral regeneration.

## 2. Results

### 2.1. Morphological characterization and mechanical properties

On the macro scale, AM Zn showed precisely controlled topology with 67% porosity (Fig. 2A). On the micro scale, AM Zn had refined grains with an average grain size of 12 μm owing to the fast cooling rate of up to $10^6$ K/s under laser melting (Fig. 2B). The compressive mechanical properties showed that AM Zn scaffold had a yield strength of 11 MPa and stiffness of 0.8 GPa, which is comparable to that of the human trabecular bone (Fig. 2C).

The chemical structure of methacrylic anhydride chondroitin sulfate (MACS) was confirmed by the $^1$H NMR spectrum (Fig. S1), which clearly shows the signals of vinyl protons at 5.65 and 6.10 ppm (a, 2H, $CH_2$), methyl protons of CS at 1.95 ppm (b, 3H, $CH_3$), and methyl protons of methacryloyl groups at 1.85 ppm (c, 3H, $CH_3$). The morphology of these hydrogels was evaluated using scanning electron microscopy (SEM) and is shown in Fig. 2D. The hydrogel revealed porous and irregular network

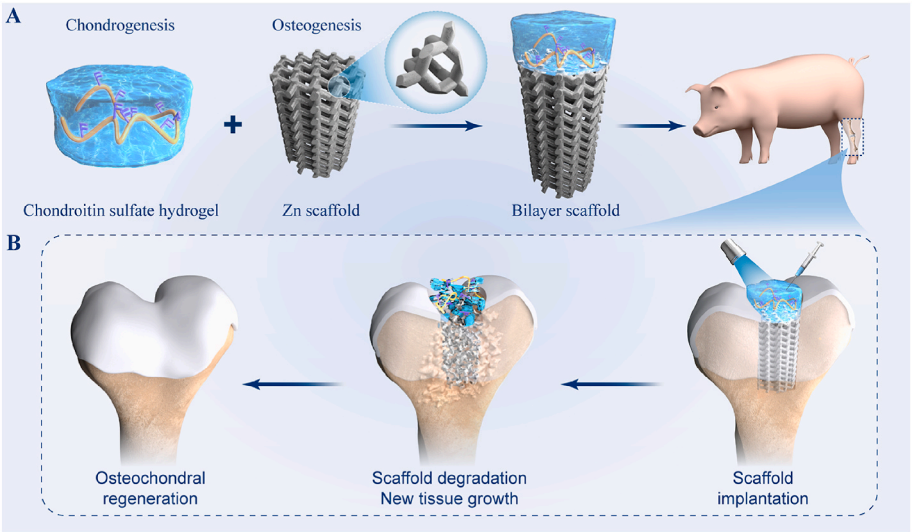


**Fig. 1.** Schematic illustration of a bilayer scaffold composed of chondroitin sulfate (CS) hydrogel and porous Zn designed to repair osteochondral defects. A) The composition of the photocuring CS hydrogel and porous Zn scaffold. B) The efficacy of the bilayer porous Zn-hydrogel scaffold in treating osteochondral defects was evaluated through an animal experiment involving Bama pigs, with the CS hydrogel on the cartilage layer and the Zn scaffold on the bone layer.

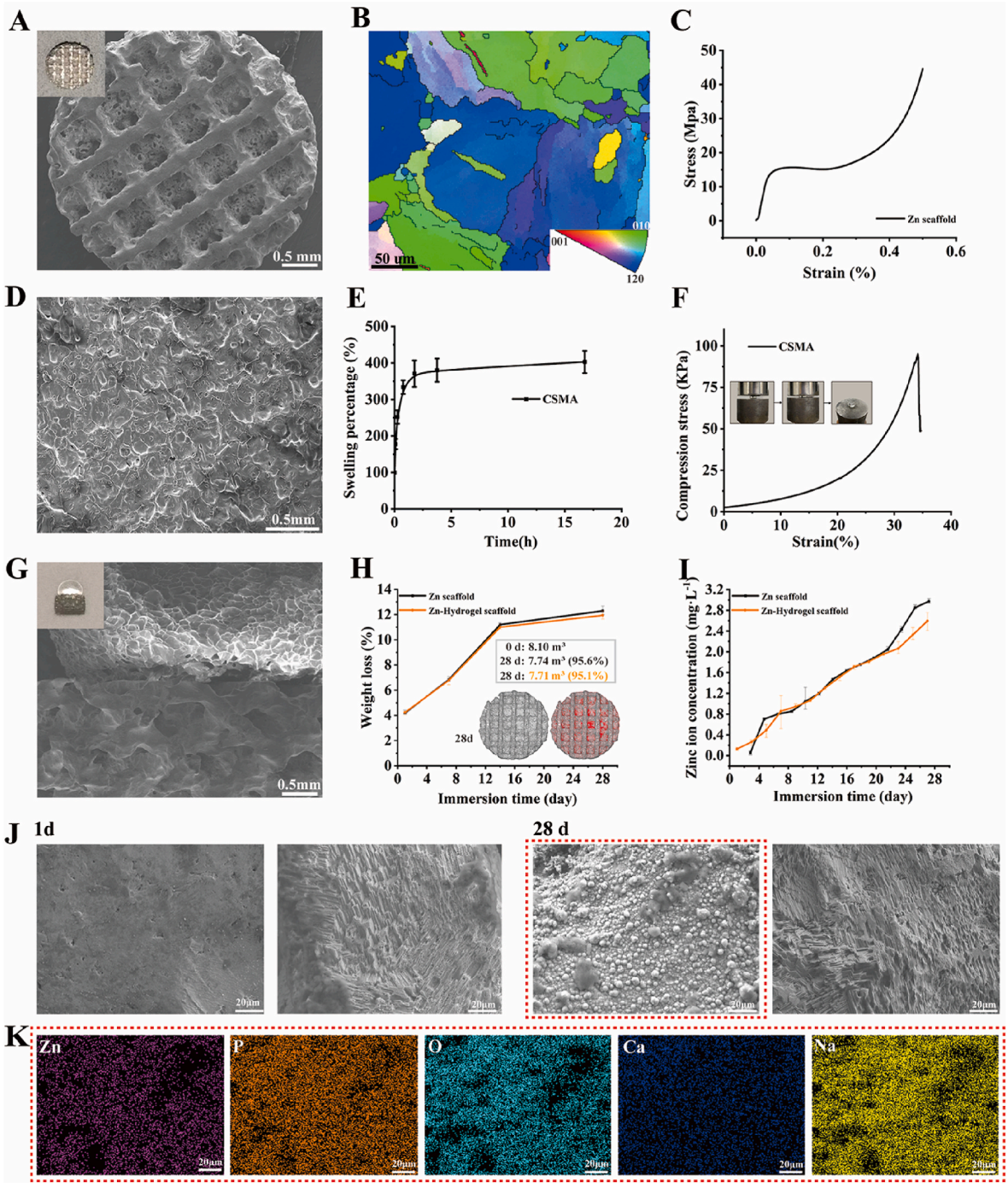


**Fig. 2.** Characterizations of the bilayer Zn-hydrogel scaffold. A) Macro and micro scales of the porous Zn scaffold; B) Electron back-scattered diffraction characterization of the porous Zn scaffold; C) Compressive stress-strain relationships of the porous Zn scaffold; D) SEM image of the MACS hydrogel; E) Swelling behavior of the MACS hydrogels in water; F) Compressive stress-strain relationships of the MACS hydrogel; G) Macro and micro scales of a combination of bilayer Zn-hydrogel scaffold; H) Weight loss and volume loss of Zn-hydrogel scaffold with immersion time (grey: Zn scaffolds, red: degradation products); I) Zn ion concentration variation with immersion time; J) SEM images of degradation products at day 1 and day 28; K) EDS mapping of the degradation layer at day 28.

structures. Fig. 2E shows the swelling behavior of the MACS hydrogels in water. The MACS hydrogel exhibited appropriate swelling behavior, reached equilibrium swelling (~400% equilibrium swelling percentage) in 2 h, and maintained a stable swelling ratio, indicating that the MACS hydrogels had good dimensional stability. The prepared MACS hydrogels also showed good mechanical performance, with a compressive strength of 82 kPa (Fig. 2F).

### 2.2. *In vitro degradation behavior*

AM Zn scaffolds and MACS were combined to form a bilayer functional Zn-hydrogel composite (Fig. 2G). The degradation behavior of the bilayer scaffolds was evaluated in a simulated body fluid. The pH value was almost constant (approximately 7.4) during the degradation, mimicking the physiological condition. The weight loss of the scaffolds increased from 4% to 12% 28 days after immersion, with no significant difference between the Zn and Zn-hydrogel scaffolds (Fig. 2H). Micro-

computed tomography (micro-CT) reconstruction showed that the volume loss after 28 days was 4.4% and 4.9% for Zn and Zn-hydrogel scaffolds, respectively, which is slightly lower than the weight loss. Zn-ion concentration also increased gradually for both specimens, while the Zn-hydrogel scaffold exhibited a slightly lower Zn-ion release at different time points (Fig. 2I). Degradation products gradually formed on the AM Zn scaffolds from day 1 to day 28 (Fig. 2J). According to the energy-dispersive X-ray spectroscopy (EDS) analysis, the degradation products mainly contained Na, O, P, and Ca (Fig. 2K). The degradation layer became more compact with a longer immersion time, while the P and Ca contents increased further. After cleaning the degradation products, the degraded area was exposed on the AM Zn surface, indicating the degradation profile (Fig. 2J).

### 2.3. Cytocompatibility

The cytocompatibility of the specimens was evaluated via the cultivation of rat bone mesenchymal stem cells (rBMSCs) with pure Zn porous scaffolds and hydrogel. The results depicted in Fig. 3A demonstrate that the viability of cells cultured in 100% Zn scaffold extract medium (20.2 ± 2.6 mg/L) was less than 75% after 24 h of cultivation, indicating a cytotoxic effect. However, with an increase in culture time to 3 and 5 days, cell viability improved to >75%. Conversely, the cells cultured in 50% and 10% extract concentrations and hydrogel exhibited high relative cell viability at different time points.

The cell morphology at different extract concentrations was observed using a laser-scanning confocal microscope. As depicted in Fig. 3B, the cell density in the 100% extract concentration was lower than that in the blank control group. Nevertheless, the cells in the 50% and 10% extract concentrations displayed desirable spreading morphologies and distinct cytoplasmic filaments. Additionally, the antennae connecting the cells were interconnected comparably to that of the blank cell culture medium group. This pattern agrees with the outcomes of the cell viability analysis. Furthermore, the rBMSCs displayed a typically fusiform cell morphology within the CS hydrogel scaffold (Fig. 3C).

### 2.4. Osteogenic and chondrogenic ability

The findings from the alkaline phosphatase (ALP) staining conducted on day 7 and alizarin red staining conducted on day 14 (Fig. 4A) indicate that the 10% pure Zn scaffold extracts facilitated the osteogenic differentiation of rBMSCs. The mRNA analysis conducted on days 7 and 14 revealed that the Zn-10% extract group exhibited higher ALP, OCN, ColI, and Runx2 expression than the blank control group (Fig. 4B–E). These results provide evidence for the in vitro osteogenic potential of the pure Zn scaffold. Furthermore, the Zn-10% extract eluate did not exhibit in vitro chondrogenic effects (Fig. S2).

To assess the chondrogenesis of the hydrogel in vitro, we evaluated the expression of chondrogenic genes (Fig. 4F–H). No significant difference was observed between groups in the expression of ACAN, SOX9, and Col II on day 7. However, on day 14, the hydrogel group exhibited higher expression of SOX9 and Col II in rBMSCs compared to the control group, indicating the hydrogel's potential chondrogenic ability.

### 2.5. General evaluation of the repaired knees

To identify the superiority of the developed bilayer Zn-hydrogel scaffold with both biomechanical and bioactive gradients in osteochondral repair, we conducted in vivo evaluations using a porcine model by creating cylindrical defects (diameter: 4.0 mm; depth: 8.0 mm) at the knee joint trochlear site. Three groups were investigated: the control group with microfracture (MF), the single hydrogel scaffold group, and the Zn-hydrogel scaffold group. As shown in Fig. 5A, the application of 3.0T MRI demonstrated that the control group exhibited incomplete filling of defects at 12 weeks post-surgery. The hydrogel scaffolds group displayed partial filling, albeit not reaching the joint surface, while the Zn-hydrogel scaffolds group exhibited complete cartilage filling with a smooth surface. After 24 weeks, the defects in the control group had decreased in size, the hydrogel scaffolds group displayed irregular defect

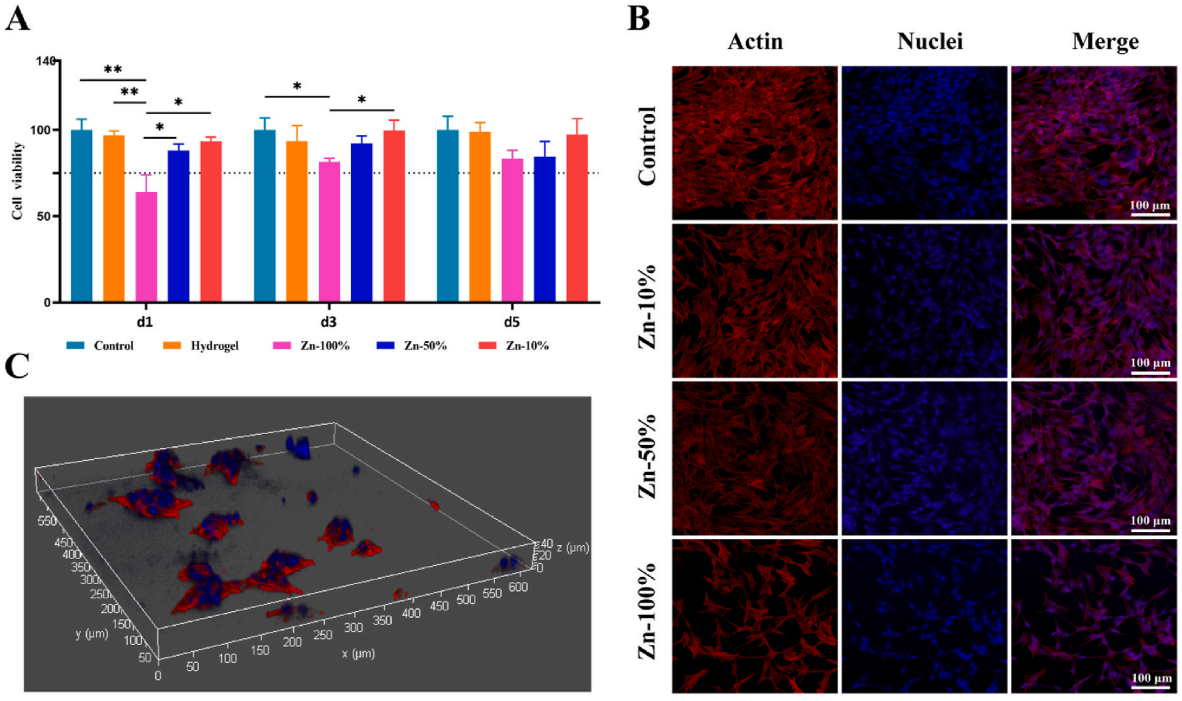


**Fig. 3.** Cytocompatibility of pure Zn porous scaffold extracts and hydrogel. A) In vitro cytotoxicity test of rBMSCs cultured in pure Zn porous scaffolds with and without dilution; B) Laser scanning confocal microscopy images of rBMSCs cultured in pure Zn porous scaffold extracts with and without dilution; C) 3D images of the spreading morphology for rBMSCs on CS hydrogel scaffold. The actin cytoskeletons were stained red, and the nuclei were stained blue. The data (n = 3) are expressed as mean ± standard deviation (SD). *p < 0.05, **p < 0.01.

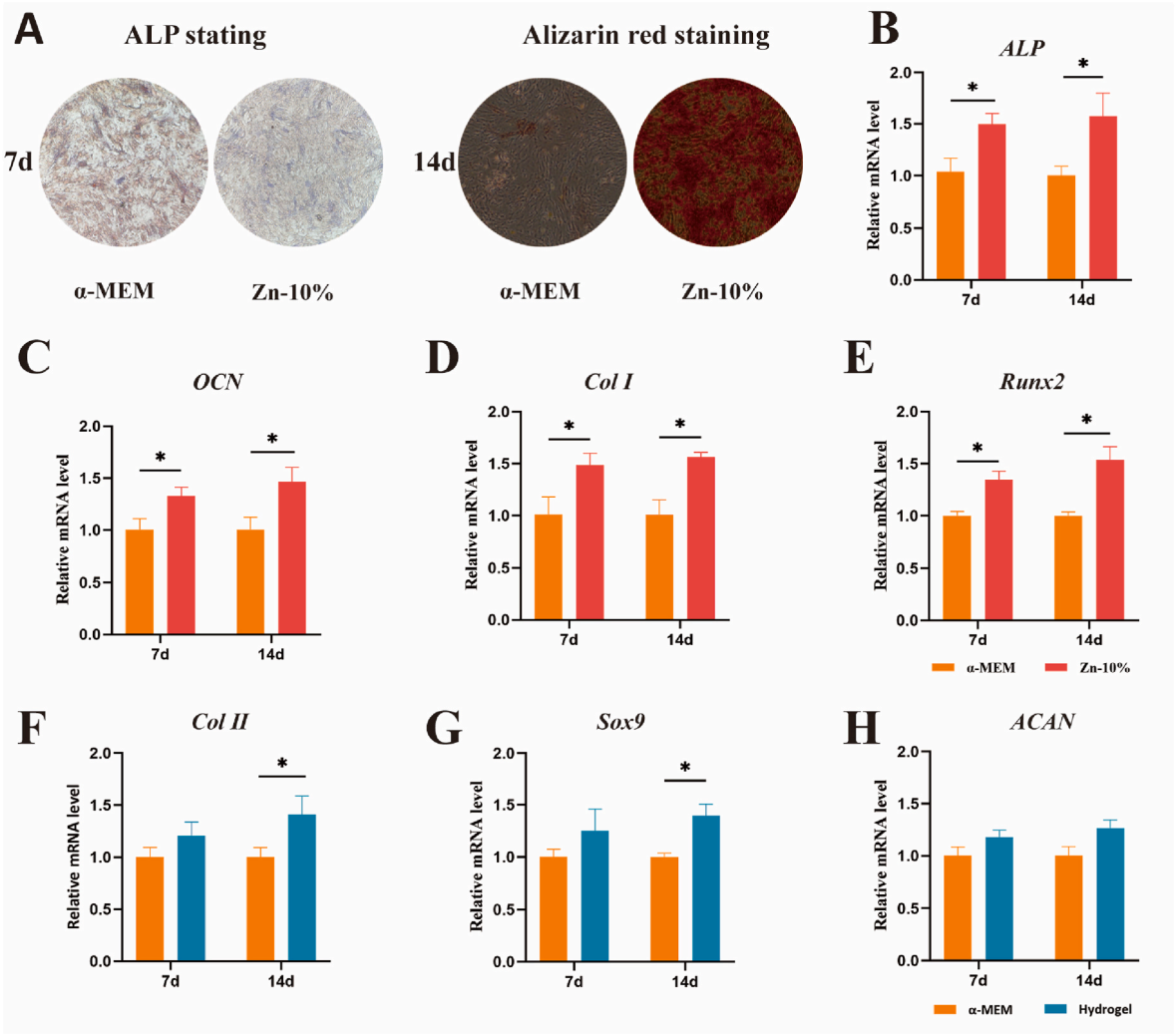


**Fig. 4.** Osteogenic capability of Zn scaffold extracts and chondrogenic capability of the hydrogel. A) Alkaline phosphatase (ALP) staining on day 7 and alizarin red staining on day 14; B-E) Expression of osteogenic genes (ALP, OCN, Runx2, and ColI) of rBMSCs on days 7 and 14; F-H) Expression of chondrogenic genes (ACAN, SOX9, and Col II) of rBMSCs on days 7 and 14. The data (n = 3) are expressed as mean ± standard deviation (SD). *p < 0.05.

filling, and the repaired cartilage in the Zn-hydrogel scaffolds group resembled normal cartilage.

Consistent with the MRI findings, gross observations (Fig. 5B) indicate that the defects in the control group remained unfilled 12 weeks post-surgery. The hydrogel scaffolds group also exhibited defects, albeit with a more comprehensive and uniform filling. In contrast, the defects repaired with Zn-hydrogel scaffolds were entirely filled, albeit with a thinner repair tissue compared to the adjacent normal cartilage. At 24 weeks, the control group exhibited a reduction in the size and depth of their defects. Conversely, the defects treated with hydrogel scaffolds displayed a rough texture and incomplete filling, whereas the Zn-hydrogel scaffolds group demonstrated consistent and smooth cartilage repair within the defect region. Further, we applied the International Cartilage Repair Society scoring system to semi-quantitatively evaluate these macroscopic results based on Table S1 (Supporting Information). The Zn-hydrogel scaffolds group showed the best gross appearance (Fig. 5E). These findings indicate that Zn-hydrogel scaffolds can effectively fill osteochondral defects and facilitate the regeneration and remodeling of articular cartilage defects.

The quantification results of synovial inflammatory factors IL-1β and TNF-α (Fig. 5C) indicate that the inflammation response remained at preoperative levels following implantation of the biphasic scaffold, suggesting that the scaffold did not induce inflammation. Furthermore, the $Zn^{2+}$ concentration in the serum was maintained at preoperative levels (Fig. 5D), with the concentration in knee synovial fluid remaining consistently below 0.1 mg/L at all time points. These findings suggest that the pure Zn scaffold did not result in significant local or systemic $Zn^{2+}$ accumulation after implantation. The supplementary data presents images of H&E-stained sections of the organs. The results depicted in Fig. S3 indicate that the pure Zn scaffolds did not induce any significant pathological changes in the heart, liver, spleen, lungs, and kidneys 12 and 24 weeks after implantation, thus demonstrating their biosafety for the vital organs of porcine.

### 2.6. Histological assessment of repaired cartilage

At the 12-week post-surgery mark, the control group exhibited unfilled cartilage defects. While the defects were eventually filled at the 24-week mark, the resulting tissue was characterized by irregular fibrocartilage. Conversely, the hydrogel group demonstrated gradual improvement in cartilage defect filling over time, albeit with disorganized collagen fiber distribution and the absence of subchondral bone. In contrast, the Zn-hydrogel group exhibited continuous cartilage repair and regeneration, with the repaired tissue integrating seamlessly with the surrounding tissue and the emergence of subchondral bone. Furthermore, the contour of the regenerated tissue within the Zn-hydrogel scaffolds resembled that of the native cartilage (Fig. 6A). The control and hydrogel scaffold groups displayed a paucity of

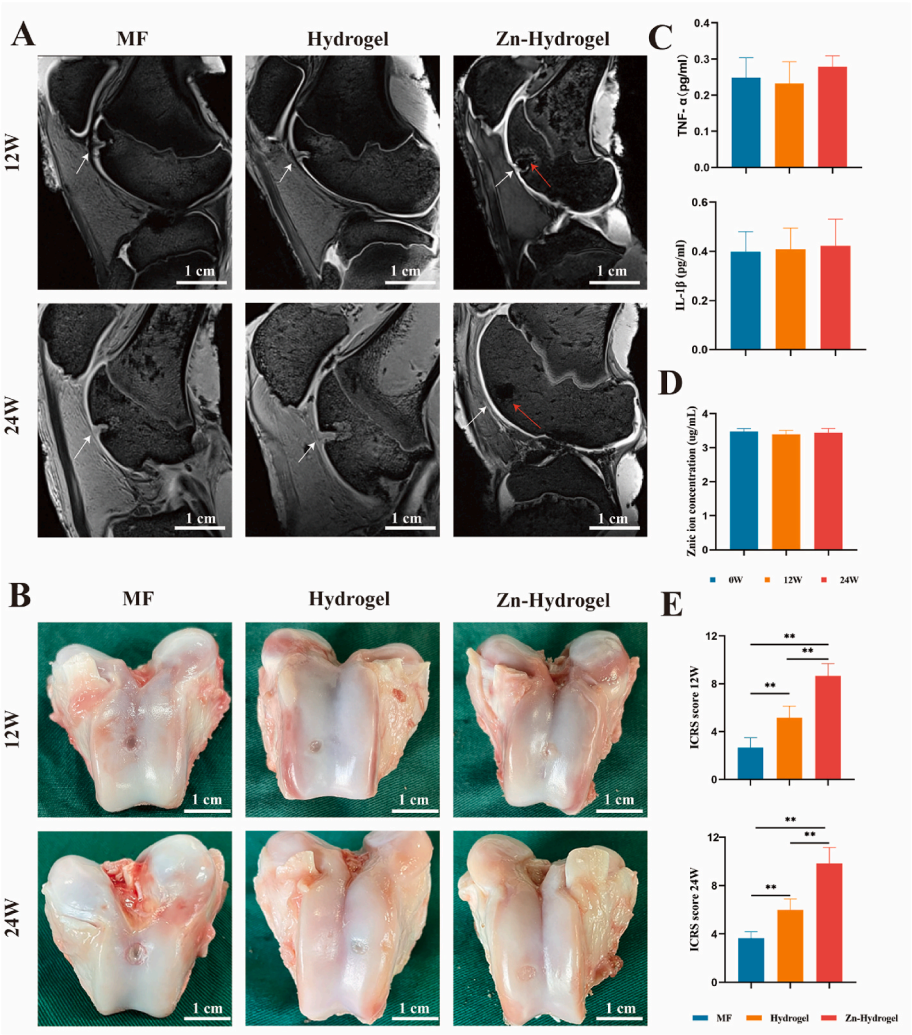


**Fig. 5.** General evaluation of the repaired knees. A) MR imaging of repaired knees at various time points (white arrow, repaired sites; red arrow, Zn scaffold); B) Macroscopic observation of the repaired cartilage defects at weeks 12 and 24; C) content of interleukin-1β and tumor necrosis factor-α in joint fluid; D) $Zn^{2+}$ concentration in the serum at various time points; E) The International Cartilage Repair Society scoring system macroscopic scores for gross observations. *$p < 0.05$, **$p < 0.01$.

chondrogenic cells occupying and sustaining the defect. Notably, the hydrogel scaffolds group demonstrated a significantly superior histological grading (Fig. 6D, Table S2).

The quality of tissue repair was evaluated using Alcian staining and immunohistochemistry for type II collagen. The semiquantitative results demonstrated that, following 12 and 24 weeks after surgery, the Zn-hydrogel group exhibited the highest level of type II collagen expression compared to the hydrogel and MF groups (Fig. S4). The results, depicted in Fig. 6B and **C**, indicate that in the Zn-hydrogel scaffold group, the distribution of repair collagen fiber is akin to the innate arrangement of the extracellular matrix (ECM). The regenerated collagen fibrils were smaller and disorganized, which was also observed in the single-layer hydrogel scaffold groups. The regenerated collagen fibers were disordered, with most of the direction of collagen fibers being consistent with the stress direction. Light staining for the cartilage-like matrix was demonstrated at 12 and 24 weeks post-surgery. In contrast, the use of Zn-hydrogel scaffolds resulted in a notable increase in the production of a cartilage-like matrix during the defect-filling process. After 24 weeks, the repaired areas treated with the Zn-hydrogel scaffolds exhibited a uniform and positive staining for cartilaginous ECM, which was comparable to that of the native cartilage. The immunohistochemical staining was consistent with the Alcian staining and demonstrated the superior quality of cartilage repair achieved using Zn-hydrogel scaffolds.

### 2.7. Biomechanical properties of repaired cartilage

Nanoindentation was used to conduct biomechanical testing on the repaired cartilage zones at the 24-week post-surgery mark. The results indicated that the Zn-hydrogel scaffold-repaired cartilage exhibited a significantly higher reduced modulus value than the control and hydrogel scaffold groups (Fig. 6E). Furthermore, the Zn-hydrogel scaffold-repaired cartilage was harder than the other two groups (Fig. 6F). Additionally, the articular surface repairs in the control and hydrogel scaffold groups were rougher than those in normal cartilage (Fig. 6G). The integration and smoothness of the cartilage surface repaired by the Zn-hydrogel scaffold demonstrated similarity to normal cartilage. Consequently, biomechanical testing revealed that the Zn-hydrogel scaffolds facilitated comparable mechanical strength to that of normal cartilage.

### 2.8. Cartilage collagen orientation and distribution

In normal cartilage, the superficial collagen fibers align parallel to the cartilage plane, whereas the collagen fibers in the base zone grow perpendicularly into the subchondral bone, as reported in previous

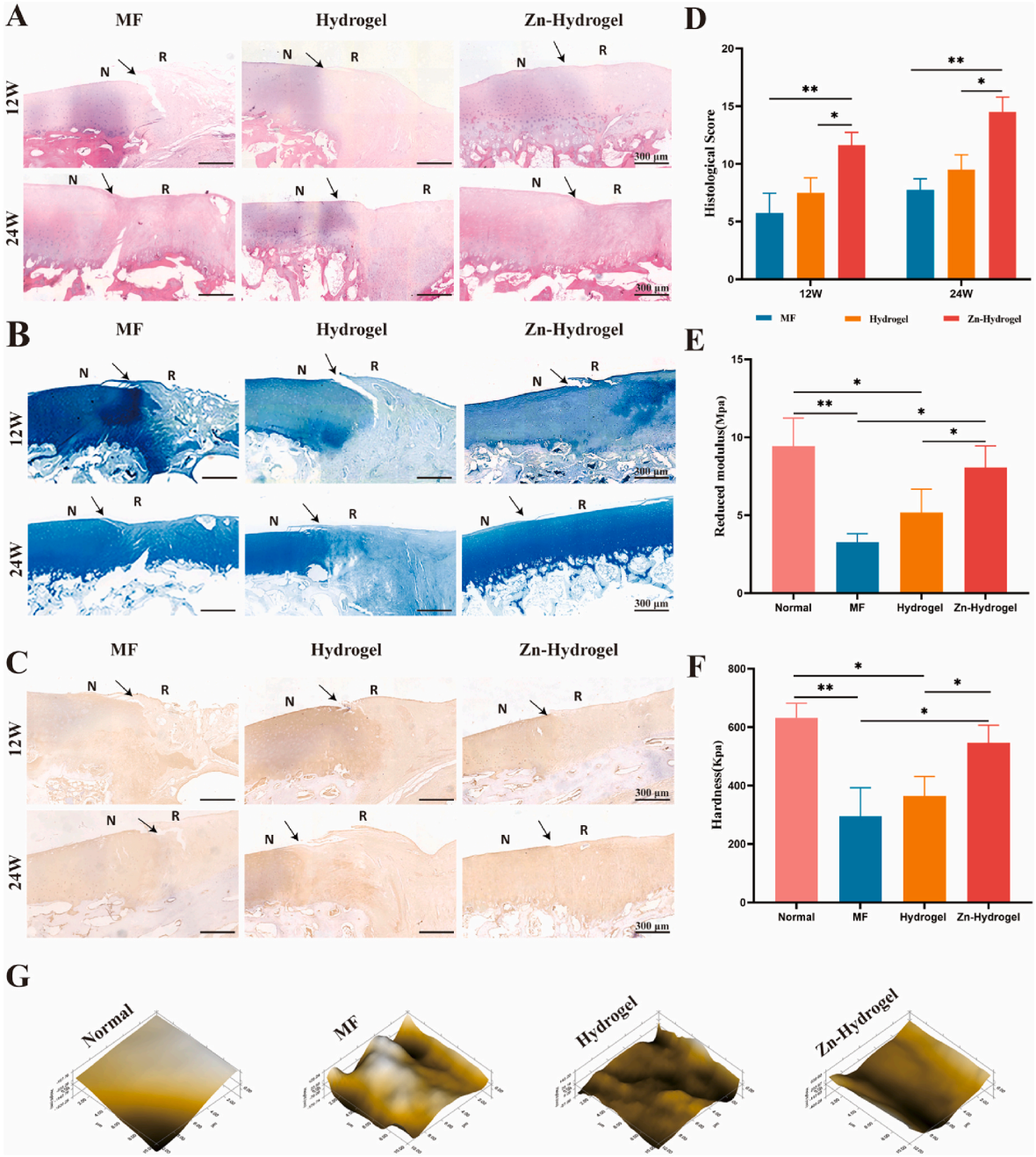


**Fig. 6.** Histological assessment and biomechanical tests of repaired cartilage in vivo. A) H&E staining of repaired cartilage at 12 and 24 weeks (N: normal cartilage; R: repair cartilage; the arrows indicate the margins of the normal cartilage and repaired cartilage); B) Alcian staining of repaired cartilage at 12 and 24 weeks; C) Immunohistological staining for collagen type II at 12 and 24 weeks; D) Histological score for repaired cartilage during in vivo implantation (n = 5). The biomechanical properties of repaired cartilage in different groups: E) reduced modulus, (F) hardness, and (G) microscopic geomorphology at 24 weeks. *p < 0.05, **p < 0.01.

studies [45,46]. The current investigation utilized picrosirius red staining to examine the orientation of collagen fibers in recently formed cartilage. Fig. 7A depicts that the distribution of collagen between the superficial and base zones in the MF and hydrogel groups did not exhibit any noticeable differences, suggesting the formation of fibrous cartilage exclusively. In contrast, the Zn-hydrogel scaffold group demonstrated a tendency for collagen fibers in the superficial zone to orient between −20° and 20°, representing 59.13% of all orientations, which is significantly higher than the 33.17% observed in the hydrogel group and 22.22% in the MF group. The findings indicate that in the base zone, the Zn-hydrogel scaffold group demonstrated a greater prevalence of collagen alignment within the 60°–90° range, with a proportion of 48.72%, in contrast to the hydrogel and MF group, which exhibited proportions of 39.94% and 28.63%, respectively (Fig. 7B). This distribution was comparable to that of the native cartilage, which exhibited proportions of 72.41% in the superficial zone and 65.67% in the base zone (Fig. 7C). The results of this study indicate that providing appropriate mechanical support during the initial stages of neo-cartilage development is essential for reinstating the orientation and dispersion of collagen within the regenerated cartilage.

### 2.9. Micro-CT analysis

The scaffold located in the trochlear groove was observed using

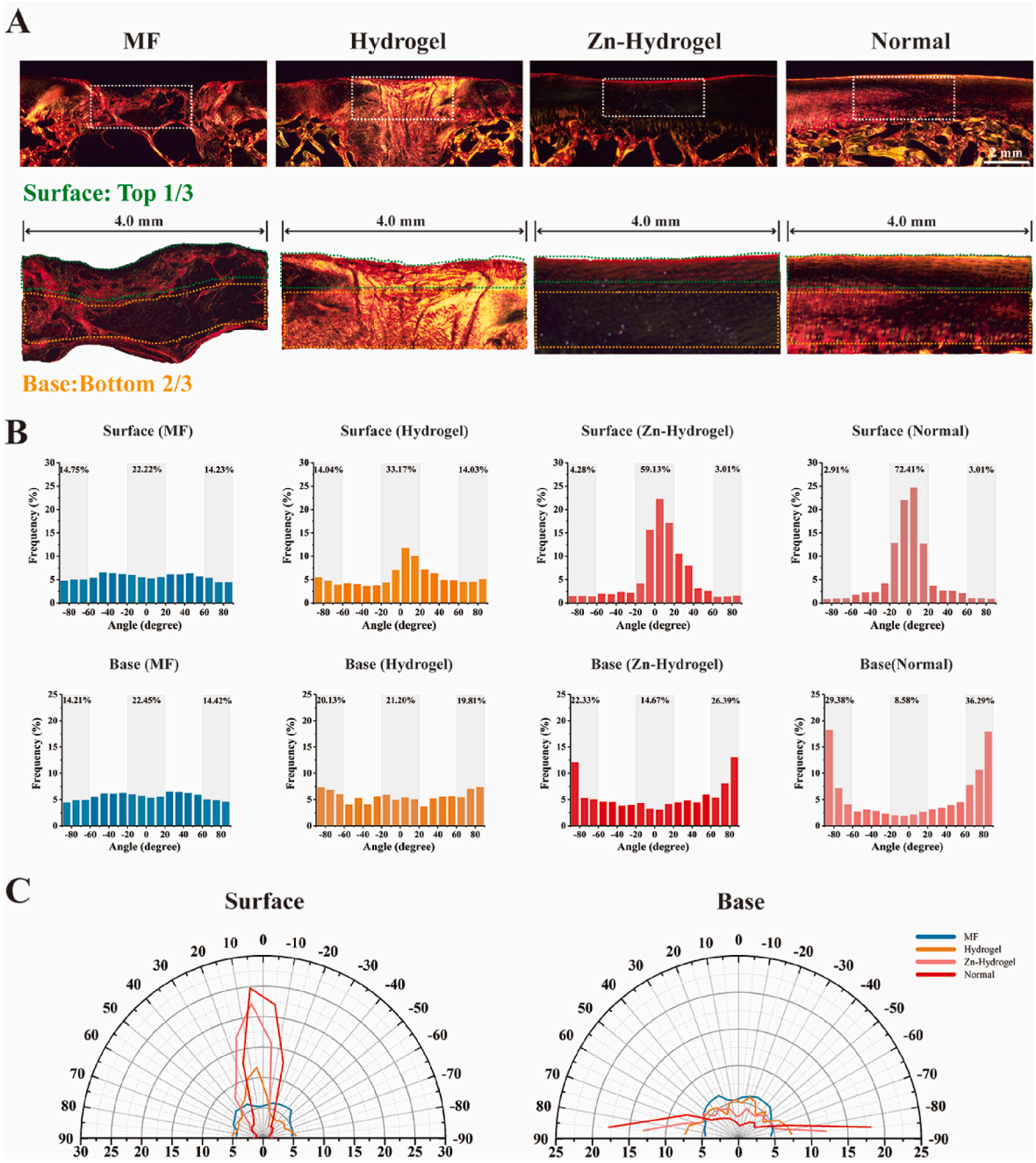


**Fig. 7.** Quantitative analyses of collagen fiber distribution of the repair tissue at 24 weeks post-surgery. A) Picrosirius red staining of regenerated tissue and normal cartilage; B) The orientation distribution in the surface area (upper 1/3) and base area (bottom 2/3); C) Polar coordinates of the surface and base areas of collagen orientation.

micro-CT to confirm the occurrence of osteogenesis in vivo. The 3D microcomputed reconstruction tomography revealed that the porous pure Zn scaffolds remained in their original position for 12 and 24 weeks without dislocation or deformation. The reconstructed images of the newly formed bone demonstrated that the osseous tissue enveloped and penetrated the internal structure of the Zn scaffolds, with greater clarity observed at the 24-week mark (Fig. 8A). The quantitative results indicated that the pure Zn scaffolds exhibited significantly higher bone volume over total volume(BV/TV) and trabec-ular thickness (Tb.Th) values at 24 weeks than at 12 weeks, which corroborated the 3D imaging characteristics. The volume of the pure Zn scaffold gradually decreased during implantation, with reductions of approximately 18.5 ± 1.1% and 27.8 ± 1.9% observed at weeks 12 and 24, respectively (Fig. 8B). These findings suggest that bone density around the implant increased over time and that bone tissue growth gradually matured at different intervals.

### 2.10. Hard tissue sections analysis

The hard tissue sections underwent staining with methylene blue/acid fuchsin and Masson's trichrome to observe the emergence of the new bone formation surrounding the porous pure Zn scaffolds (Fig. 8C). Twelve weeks after implantation, the newly formed bone matrix exhibited proximity to the Zn scaffold, with new bone growth penetrating the pores of the Zn scaffolds. At the 24-week mark, a greater amount of new bone was observed to be closely connected to and

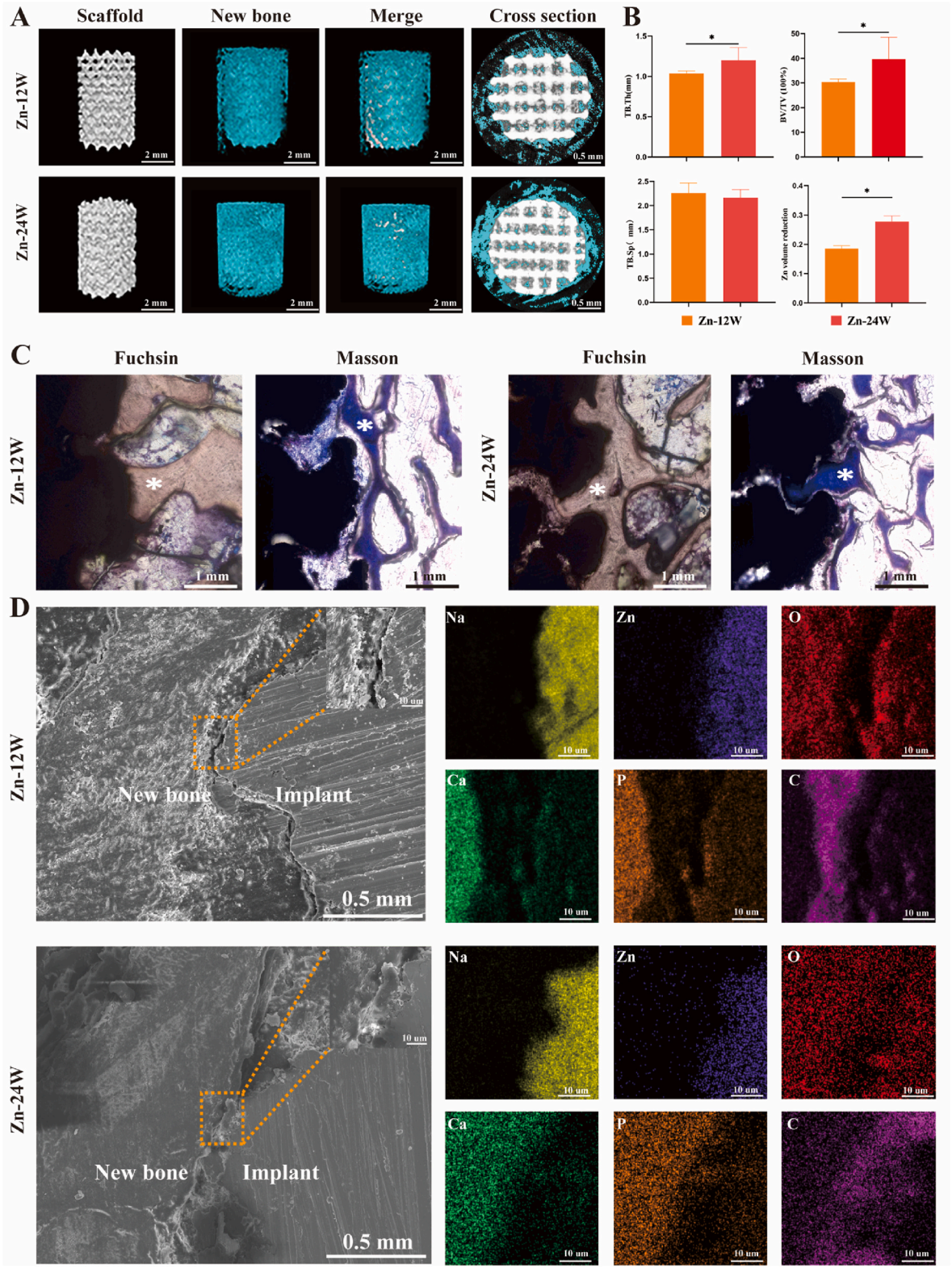


**Fig. 8.** Micro-CT images, hard tissue sections assessment, and electron images and elemental maps (SEM/EDS) of porous Zn scaffolds in vivo and newborn bone analysis at 12 and 24 weeks postoperatively. A) Reconstructed micro-CT 3D images; B) Quantitative analysis of the micro-CT data, including Tb.Th, Th.Sp, BV/TV, and Zn scaffolds volume reduction; C) Methylene blue/basic fuchsin staining and Masson's Trichrome staining at weeks 12 and 24 postoperatively, *: new bone; D) SEM images coupled EDS mapping of the hard tissue cross sections after 12 and 24 weeks, with magnified images (orange rectangles) and with corresponding elemental distribution visible. *$p < 0.05$.

growing into the pores of the pure Zn porous scaffolds. In the middle of the Zn scaffold, at 12 weeks post-implantation, a small amount of newly formed bone tissue was present within the scaffold. Subsequently, after 24 weeks, a significant increase in newly formed bone tissue was observed (Fig. S5). This trend is consistent with the results obtained from micro-CT, indicating the in vivo osteogenic capacity of Zn scaffolds.

The hard tissue section underwent sputter deposition with a thin gold film and was subsequently examined under a scanning electron microscope (S-4800, Hitachi Ltd., Ibaraki, Japan) equipped with an energy-dispersive X-ray spectrometer (QUANTAX, Bruker, Germany). This was done to analyze the alterations in the structure and composition of the degradation layer. Fig. 8D depicts the SEM and EDS images of the porous Zn scaffolds 12 and 24 weeks after implantation. The pure Zn porous scaffold exhibited a uniform degradation pattern, with the Zn scaffolds surrounded by a significant and dense layer of newly formed bone. The degradation product layer that covered the pure Zn scaffolds was primarily composed of Na, Zn, O, Ca, and P.

## 3. Discussion

Due to the distinctive characteristics and reparative potential of chondral and osseous tissues, respectively, it is widely acknowledged that osteochondral defect regeneration is challenging. In this study, a biocompatible multifunctional biodegradable bilayered scaffold with gradients of biomechanical properties was successfully developed to facilitate the regeneration of osteochondral tissue in a porcine osteochondral defect model. Our findings demonstrate that the Zn-hydrogel scaffold significantly enhanced osteochondral regeneration, underscoring the need for an osteochondral scaffold to be able to concurrently promote chondral and osseous regeneration.

The compressive modulus of a typical osteochondral tissue increases from the chondral to the osseous aspect, rendering single-layer scaffolds insufficient in fulfilling the requisite biomechanical criteria [47]. The spatial distribution of repaired cartilage collagen fibers in the Zn-hydrogel group exhibited a remarkable resemblance to the natural organization of the ECM. Conversely, the regenerated collagen fibrils in the hydrogel group were characterized by their diminished size and disordered arrangement. Results obtained from the in vivo study of microfracture and implantation using a single hydrogel scaffold demonstrate that, without appropriate biomechanical implants at the bone layer, the chondral layer cannot withstand the considerable levels of compressive and shear loading typically occurring in articulating joints post-implantation. Despite the filling of osteochondral defects with a blood clot containing bone marrow-derived mesenchymal stem cells, the gradually maturing clot remained susceptible to joint stress in the early phase owing to the lack of mechanical support by a bony layer [48–50]. These results indicate that proper early mechanical support during neo-cartilage formation is crucial for achieving optimal repair efficacy [51].

Bilayered scaffolds exhibiting gradient mechanical properties in each component represent the most biomimetic alternatives for restoring osteochondral defects [52]. Numerous researchers have endeavored to produce bilayer scaffolds comprising metals at the bone layer to provide mechanical support for cartilage regeneration [53]. Yang et al. [16] produced a biphasic poly-lactic-co-glycolic acid 3D-printed Ti6Al4V scaffold for cartilage and bone regeneration. Similarly, Duan et al. [17] investigated the efficacy of a biphasic hydrogel-Ti6Al4V scaffold in restoring osteochondral lesions, utilizing porous Ti6Al4V as an osseous phase. Wei et al. [18] developed collagen membranes with a porous tantalum scaffold to address osteochondral defects. Although these bone layer composites offer mechanical support, their compressive strengths (43.04−73 MPa) exceed those of cancellous bone. Furthermore, while the utilization of 3D printing had allowed for the creation of porous designs of metal implants aimed at reducing their elastic moduli, with this technological advancement, the elastic modulus of porous titanium can be minimized to 15.4 GPa [54], while porous tantalum can be reduced to 3.0 GPa [55]. However, it is important to acknowledge that these values still remain significantly higher than the elastic modulus of cancellous bone (less than 0.3 Gpa) [20]. In the present study, the AM Zn scaffold demonstrated an elastic modulus of 0.8 GPa, a value that closely corresponds to that of cancellous bone. Moreover, while nondegradable materials at the osseous phase can offer mechanical support, they lack functional support for osteochondral interfaces. These materials cannot replicate the interfacial zone and exhibit limited osteogenesis compared to Zn scaffolds [56–60]. The presence of calcified cartilage at the interfacial zone is essential for integrating soft and hard tissue and distributing mechanical loads across the interface [8,61,62]. Additionally, the non-degraded material may persist and necessitate surgical removal [63]. The findings from the in vivo implantation of the Zn scaffold provide evidence that with appropriate biomechanical implants at the bone layer, hydrogels at the chondral layer can effectively endure the significant compressive and shear loading characteristic of an articulating joint following implantation.

The results of this in vivo investigation indicate that the newly formed bone was in proximity to the Zn scaffold and had grown into its pores, as revealed by histological staining. Moreover, micro-CT analysis demonstrated that the Zn scaffold exhibited higher BV/TV and Tb.Th values at 24 weeks compared to 12 weeks. The intense deposition of Ca and P surrounding the Zn scaffold further suggests that it significantly accelerated the formation of new bone induced by pure Zn and its degradation products [64,65]. The porous Zn scaffold exhibited a reduction of approximately 27.8% at 0.5 years post-operation, with complete degradation potentially occurring within 2 years. The optimal degradation rate for bone implants is typically within 1–2 years [23,30]. Therefore, the porous Zn scaffold is a promising candidate for bone regeneration, offering adequate mechanical support for the cartilage layer.

The findings of the in vitro cell viability assessment suggest that the pure Zn scaffold extracts, at 50% and 10% concentrations, demonstrated favorable cytocompatibility and a stimulating impact on rBMSCs cell proliferation compared to the 100% extracts. Previous research has recommended a minimum dilution of 6–10 times for degradable metal extracts in cytotoxicity testing, as bodily fluids rapidly dilute the degradation products [66]. Notably, $Zn^{2+}$ has been observed to have biphasic effects on living organisms [67]. Low concentrations of $Zn^{2+}$ are believed to promote the proliferation, adhesion, and differentiation of osteogenic cells, while high concentrations of $Zn^{2+}$ have the opposite effect [58]. A previous study found that the osteogenic effect of $Zn^{2+}$ on SaOS-2 cells was reversed when the extracellular ionic concentration exceeded 1.6 μg/ml [67]. Another study demonstrated that $Zn^{2+}$ concentrations above 130 μM resulted in a diminished stimulatory effect and increased cytotoxicity on mouse MC3T3-E1 cells. The present study's findings indicate that the 100% pure Zn scaffold extracts (20.2 μg/ml) exhibit toxicity towards rBMSCs cells in vitro, as evidenced by the results of cell viability and cytocompatibility tests. However, when the extracts were diluted to 50% and 10%, the cell viability was >85%, indicating that the biocompatibility of the pure Zn scaffold was safe in vitro. Additionally, the 10% pure Zn scaffold extracts demonstrated osteogenic capacity in vitro, as evidenced by the higher expression of ALP, COL1, OCN, and RUNX2 compared to that in the blank control. Prior research has demonstrated that $Zn^{2+}$ can penetrate BMSCs, triggering the cAMP-PKA-MAPK pathway within the intracellular environment [68,69]. This phenomenon is further compounded by the ability of intracellular $Zn^{2+}$ to augment the transcription of Runx2 and the expression of ALP and OCN, thereby promoting osteogenic differentiation in BMSCs [70]. In light of these findings, the present in vivo investigation substantiates the osteogenic potential of pure Zn scaffolds for bone regeneration.

This study has certain limitations. Firstly, due to limitations in the number of specimens, additional quantitative data related to bone regeneration should be included in future studies. Moreover, challenges

exist in the subsequent application of these new biodegradable scaffolds. Therefore, future studies should focus on evaluating the physiological and mechanical properties of the Zn scaffold for longer periods of approximately 2 years, until the scaffold is fully degraded. Lastly, further exploration is required to elucidate the detailed osteogenic mechanisms of pure Zn scaffolds.

## 4. Conclusion

This study introduces a novel methodology for fabricating osteochondral scaffolds that facilitate osteochondral regeneration. Our approach entails the utilization of methacryloyl CS hydrogel and bioactive biodegradable metal as the cartilage and bone layers, respectively. The porous structure of the bioactive biodegradable metals, particularly Zn, can be attained through AM, which augments bone tissue regeneration and furnishes mechanical reinforcement akin to that of cancellous bone in the initial phases of cartilage regeneration. The bilayer scaffold exhibited favorable biocompatibility and facilitated the expression of chondrogenic and osteogenic differentiation-related genes in vitro. The in vivo experiments conducted on large animals demonstrated the potential of the fully degradable bilayer scaffold as a promising treatment for repairing osteochondral defects owing to its biomechanical and bioactive gradients. It is anticipated that the bilevel hydrogel-biodegradable metal scaffold will serve as a valuable platform for regenerative medicine.

## 5. Experimental section

### 5.1. Synthesis of methacryloyl chondroitin sulfate (MACS)

MACS was synthesized according to previous publication with some modification [1]. Briefly, 1 g of CS powder was completely dissolved in deionized water (100 mL). Subsequently, 15 g methacrylic anhydride (MA) was dropwise added to the CS solution. The pH of mixture solution was regulated to ~8.0 by employing 5 M NaOH solution. Then the mixture solution was allowed to react at ambient temperature for 2 h and at 6 °C for another 24 h. The resulting solution was precipitated in alcohol and washed with excess alcohol several times. The prepared MACS was dried in a vacuum oven at room temperature. 1H NMR spectra of MACS were recorded using a JEOL JNM-ECA 600 (600 MHz) with D2O as solvent.

### 5.2. Swelling behavior of MACS hydrogels

Cylindrical MACS hydrogels were individually weighted (S0) and incubated in deionized water at ambient temperature for 17 h. At predetermined intervals, the hydrogels were carefully taken out, the residual water on hydrogel surface was drained by filter papers and weighed (S1). The swelling percentage (SP) was determined with equation (1):

$$SP = S_1/S_0 \times 100\% \quad (1)$$

Mechanical properties of these hydrogels were tested using a universal mechanical testing machine (WDW3020, China) with a 1 kN load cell at a cross-head speed of 5 mm min−1.

### 5.3. Zn scaffold fabrication

4*6 mm cylindrical scaffolds with a diamond unit cell (unit cell size: 1.4 mm, strut thickness: 0.4 mm) were produced by laser powder bed fusion AM (Aconity, Germany). A nitrogen-atomized Zn powder with 15–53 μm particle size was used in this study. The powder layer thickness was 30 μm and the energy density 40 J/mm3. After printing and removing the specimens from the baseplate, 96% ethanol was used to ultrasonically remove powder particles entrapped in the pores of the specimens for 20 min. Subsequently, the specimens were cleaned by using a solution composed of 5% (by volume) hydrochloric acid, 5% nitric acid, and 90% ethanol for 2 min, after which 96% ethanol was used again to wash away residual acid.

In vitro, the photocured CS scaffold and Zn scaffold demonstrate robust integration, resulting in a cohesive architecture that retains a strong connection even under the influence of gravity (Fig. S6).

### 5.4. Microstructure of AM Zn

Electron back-scattered diffraction (EBSD) was conducted with an HKL Nordlys II detector, attached to a field emission gun scanning electron microscope (FEGSEM) (JEOL JSM-6500 F, Japan), at 200 nm step size. Channel 5 software was used to reconstruct inverse pole figure (IPF) maps. The average grain width was calculated by using the line intercept method, according to ASTM E112-12. EBSD specimens were ground, mechanically polished up to 1 μm with lubricant.

### 5.5. Mechanical properties

Compression tests were carried out at 2 mm/min (10 kN, Instron, Germany). The yield strengths and stiffness of the AM porous Zn specimens were determined according to ISO 13,314:2011. The tests were performed in triplicate.

### 5.6. In vitro degradation

Static in vitro immersion tests were performed inside a beaker using simulated body fluid (SBF) for up to 28 days. Medium pH values were registered (InLab Expert Pro-ISM, METTLER TOLEDO, Switzerland) at 1, 2, 7, 14, and 28 days of degradation. An inductively coupled plasma optical emission spectroscope (ICP-OES, iCAP 6500 Duo, Thermo Scientific, USA) was used to determine the concentrations of Zn ions in the medium. Weight loss were determined by cleaning the degradation products with CrO3. All the tests were performed in triplicate.

The morphologies and compositions of the degradation products were analyzed using a scanning electron microscope equipped with an energy-dispersive X-ray spectroscope (EDS) (SEM, JSM-IT100, JEOL, Japan).

### 5.7. Cell viability and cytocompatibility assay

A preparation of Pure Zn scaffolds extracts was conducted by incubating the scaffolds in α-minimal essential medium supplemented with 10% fetal bovine serum for 24 h, at an extraction ratio of 1.0 cm2/mL, in a cell incubator maintained at 5% CO2, 95% humidity, and 37 °C. The ion concentrations were quantified using ICP-OES, while the cell viability was assessed using the CCK-8 assay (Dojindo Laboratories, Japan). Specifically, rBMSCs at passage 3 (7 × 104 cells/100 μl) were seeded in 96-well plates with various scaffold extracts (100%, 50%, and 10%), hydrogel, and basal medium as a control, with three replicates per condition. Following a culture period of 1, 3, and 5 days, the alloy extracts were extracted and supplemented with 10 μL of CCK-8 solution in each well. The cells were subsequently incubated for 2 h, and the absorbance of each well was measured at 450 nm using an ELISA reader (Molecular Devices, USA).

To investigate the impact of pure Zn scaffold extracts and hydrogel on cell morphology, cells were cultured in confocal small dishes for 24 h. Subsequently, they were gently washed with a phosphate buffered saline (PBS) solution and fixed with 4% paraformaldehyde for 30 min. The cells were then rinsed twice with PBS for 3 min each time. Cytoskeletal staining was performed using Actin-Tracker Red 594 (Biyuntian, Shanghai, China) for 30 min, followed by two additional PBS rinses. Nuclei were counterstained with Hoechst 33342 (Thermo Fisher Scientific, USA) for 15 min. Finally, specimens were observed under a laser scanning confocal microscope (Zeiss Axiovert 650, Oberkochen, Germany).

### 5.8. Alkaline phosphatase (ALP), alizarin red (AR) staining, and gene expression analysis

In order to assess the impact of Zn scaffold extracts on the initial stages of osteogenic differentiation, rBMSCs were cultivated in 12-well plates with the aforementioned extracts. After 7 days, the cells were immobilized and subjected to qualitative imaging using the BCIP/NBT ALP Color Development Kit (Beyotime, China). Following this, at 14 days, the cells were fixed in 4% paraformaldehyde and subjected to alizarin red (AR) staining (Cyagen, China) to quantify calcium deposition.

Real-time polymerase chain reaction (RT-PCR) analysis was employed to quantify the expression of bone formation-related genes (Col 1, OCN, ALP, and RUNX2) of rBMSCs in 10% extracts and cartilage-specific genes in hydrogel (SOX9, acan, and colII) at days 7 and 14. The ABI 7300 RT-PCR system (Applied Biosystems, CA, USA) was utilized for this purpose. The relative expression changes in the target genes were determined by normalizing their expression to that of 18s RNA using the ΔΔCt method. The primer sequences used in this study are provided in Table S3.

### 5.9. Animal surgery procedure

A total of eighteen male Bama mini experimental pigs, aged 6 months and weighing between 25 and 30 kg, were subjected to bilateral surgery. The pigs were anesthetized intravenously with propofol at a rate of 20 drops per minute during the operation, and the skin was disinfected using iodine and alcohol. The knee joint was exposed by dislocating the patella, and bilateral osteochondral defects measuring 4 mm in diameter and 6 mm in depth were created on the trochlear groove using a trephine. The control group utilized marrow blood to mobilize and achieve the microfracture technique. The hydrogel scaffold group involved the application of light-cured hydrogel into the osteochondral defect, which was then photocured by blue light (405 nm) for 30 s. The Zn-hydrogel scaffold group involved the implantation of pure Zn scaffolds into the bone defects, followed by the application of light-cured hydrogel onto the surface of the Zn scaffold, which was then photocured by blue light (405 nm) for 30 s. The thickness of the CS hydrogel in the bilayer scaffold was approximately 2–3 mm, which is similar to native cartilage. All implants were placed at the same level as the adjacent cartilage surface (Fig. S7). Finally, the periarticular soft tissues and skin were separately sutured with nonabsorbable 3-0 sutures (Ethicon, New Jersey, USA). The pigs were permitted to recuperate without any weightbearing constraints or immobilization following the surgery. Antibiotic prophylaxis (intramuscular injection of penicillin at a dosage of 500 mg twice daily) was administered for a duration of 5 days. At the conclusion of 12 or 24 weeks postoperatively, the animals were euthanized using pentobarbital sodium.

### 5.10. Synovial fluid and serum analysis

Synovial fluid was collected at various time points through the use of a 1 mL syringe equipped with an 18-gauge needle and subsequently centrifuged at 3000 rpm for 15 min at 4 °C. The concentrations of Interleukin-1β (IL-1β) and tumor necrosis factor-α (TNF-α) were determined through the utilization of standard ELISAs (Pig IL-1β ELISA Kit, SEA563Po; Pig TNF-a ELISA Kit, SEA133Po; Cloud-Clone Corp, Wuhan, China). Prior to surgery and at 12 and 24 weeks postoperatively, pig ear arterial blood was collected. The concentrations of $Zn2+$ in both the serum and synovial fluid were measured through the use of ICP-OES.

### 5.11. Cartilage magnetic resonance imaging

At 12 and 24 weeks following surgery, MRI analysis was conducted on each knee in the experimental groups to detect any new cartilage growth. The analysis was performed using a Siemens TIM Trio 3T MRI scanner (Siemens, Erlangen, Germany) and a small animal-specific knee coil (Chenguang Medical Technologies Co., Ltd, Shanghai, China) was utilized to enhance the signal-to-noise and contrast-to-noise ratios. The total acquisition time for the analysis was approximately 35 min, involving five sequences.

### 5.12. Micro-CT evaluation

To assess the degradation of pure Zn and Ti6Al4V scaffolds and the healing of bone defects, Micro-CT scanning was conducted at 12 and 24 weeks post-surgery. The Micro-CT device utilized for this study was the Siemens INVEON MM from Germany, with the following settings: 80 kVp, 500 μA, and 1500 ms. The INVEON workplace software from Siemens, Germany was used to calculate the Zn scaffold volume reduction and trabecular parameters, including bone volume over total volume (BV/TV), trabecular thickness (Tb.Th), and trabecular separation (Th.Sp).

### 5.13. Macroscopic morphological and histological analysis

Each knee underwent a gross examination to assess defect filling, tissue integration, and surface smoothness. The International Cartilage Repair Society Scoring System (ICRS) macroscopic scores were utilized to compare gross morphology score comparison among groups. Histological specimens were cleansed with PBS and subsequently fixed in 4% paraformaldehyde (pH 7.4) for a duration of 48 h. The hard tissue sections underwent dehydration in a graded ethanol series and polymerization in polymethylmethacrylate resin, followed by embedding in methylmethacrylate (MMA). Subsequently, the MMA blocks were sectioned into 200 μm slices using an EXAKT 300CP and polished to a thickness of 100 μm. The sections were then subjected to staining with methylene blue/acid fuchsin and Masson's trichrome to facilitate the observation of the contact area between bone and implant scaffolds. The MMA sections underwent gold sputtering via an ion sputter coater (Hitachi MC10 0 0, Japan) and were subsequently subjected to SEM/EDS characterization. The working distance and accelerating voltage utilized were 10 mm and 15 kV, respectively.

Paraffin sections were prepared by decalcifying samples in 20% EDTA (pH 7.2), followed by dehydration in a graded series of ethanol and embedding in paraffin. Serial sagittal sections, 5 mm in thickness, were obtained from the center of the repair site and subjected to staining with hematoxylin & eosin (HE), Alcian, and immunostaining of collagen type II antibody (Novabiochem, USA) using established protocols. The histological repair of articular cartilage defects was evaluated quantitatively using a standardized grading scale.

### 5.14. Nanoindentation assessment

Biomechanical testing of the repaired cartilage zones was conducted at 24 weeks post-surgery, wherein samples were obtained from the central part of the repaired tissues and normal cartilage. The samples were maintained in a hydrated state through the use of a circumfluent PBS solution. All indentations were carried out using the TriboIndenter (Hysitron Inc., Minneapolis, MN, USA) equipped with a 400-mm radius curvature conospherical diamond probe tip. A trapezoidal load function was applied to each indent site, with loading (10 s), hold (2 s), and unloading (10 s) phases. The indentations were force-controlled, with a maximum indentation depth of 500 nm. Meanwhile, the microscopic geomorphology of the indentation zones was captured using microscanning apparatus.

### 5.15. Collagen orientation and distribution analysis

The collagen network of cartilage was subjected to picrosirius red staining and examined under polarized light microscopy (BX-45, Olympus, Hamburg, Germany). The current study utilized the ImageJ

software package with Directionality plugins to ascertain the orientation distribution of collagen fibers in recently formed cartilage. The research concentrated on determining the primary angle of collagen fiber orientation in two specific regions, namely the superficial zone (which constitutes one-third of the total thickness) and the base zone (which constitutes two-thirds of the total thickness), in accordance with the native cartilage structure. Specifically, the superficial collagen fibers were found to align parallel to the cartilage plane, while the collagen fibers in the base zone grew perpendicularly into the subchondral bone.

### 5.16. Statistical analyses

All statistical analyses were performed using SPSS 26.0 statistical software (IBM Corp). The differences between each group were analyzed using an independent sample *t*-test and one-way analysis of variance (ANOVA). Data were recorded as mean ± standard error. $P < 0.05$ was considered statistically significant.

## Declaration of competing interest

The authors declare no conflict of interest.

## Data availability

Data are available from the authors upon request.

## Ethics approval and consent to participate

The Biomedical Ethics Committee of Peking university approved all animal experiments (LA2021295).

## CRediT authorship contribution statement

**Fan Yang:** Formal analysis, Data curation, Writing – original draft. **Yageng Li:** Data curation, Writing – original draft. **Lei Wang:** Data curation, Writing – original draft. **Dong Jiang:** Supervision, Funding acquisition, Writing – review & editing. **Hongjie Huang:** Supervision, Funding acquisition, Methodology. **Jianquan Wang:** Methodology, Validation, Investigation, Resources, Project administration, Funding acquisition.

## Acknowledgements

This work was supported by grants from the National Natural Science Foundation of China (grant numbers: 82072403, 82072428, 82272571, 82267020, 82372418, 52201294). Beijing Natural Science Foundation Haidian Original Innovation Joint Fund Frontier Project (L212052). Beijing Natural Science Foundation (L212014). Prosperos project, funded by the Interreg VA Flanders – The Netherlands program, CCI Grant No. 2014TC16RFCB04 and the Interdisciplinary Centre for Clinical Research (IZKF) of the Faculty of Medicine of the RWTH Aachen University (OC1-1). Holger Jahr and Jianquan Wang contributed equally to this paper.

## Appendix A. Supplementary data

Supplementary data to this article can be found online at https://doi.org/10.1016/j.bioactmat.2023.10.014.

## References

[1] L. Andriolo, C. Candrian, T. Papio, A. Cavicchioli, F. Perdisa, G. Filardo, Osteochondritis dissecans of the knee - conservative treatment strategies: a systematic review, Cartilage 10 (3) (2019) 267–277, https://doi.org/10.1177/1947603518758435.

[2] W. Shi, M. Sun, X. Hu, B. Ren, J. Cheng, C. Li, X. Duan, X. Fu, J. Zhang, H. Chen, Y. Ao, Structurally and functionally optimized silk-fibroin-gelatin scaffold using 3D printing to repair cartilage injury in vitro and in vivo, Adv. Mater. 29 (29) (2017), https://doi.org/10.1002/adma.201701089.

[3] L. Zhang, W. Dai, C. Gao, W. Wei, R. Huang, X. Zhang, Y. Yu, X. Yang, Q. Cai, Multileveled hierarchical hydrogel with continuous biophysical and biochemical gradients for enhanced repair of full-thickness osteochondral defect, Adv. Mater. 35 (19) (2023), e2209565, https://doi.org/10.1002/adma.202209565.

[4] D. Algul, H. Sipahi, A. Aydin, F. Kelleci, S. Ozdatli, F.G. Yener, Biocompatibility of biomimetic multilayered alginate-chitosan/β-TCP scaffold for osteochondral tissue, Int. J. Biol. Macromol. 79 (2015) 363–369, https://doi.org/10.1016/j.ijbiomac.2015.05.005.

[5] Y.X. Lin, Z.Y. Ding, X.B. Zhou, S.T. Li, M. Xie de, Z.Z. Li, G.D. Sun, In vitro and in vivo evaluation of the developed PLGA/HAp/Zein scaffolds for bone-cartilage interface regeneration, Biomed, Environ. Sci. 28 (1) (2015) 1–12, https://doi.org/10.3967/bes2015.001.

[6] A. Bernstein, P. Niemeyer, G. Salzmann, N.P. Südkamp, R. Hube, J. Klehm, M. Menzel, R. von Eisenhart-Rothe, M. Bohner, L. Görz, H.O. Mayr, Microporous calcium phosphate ceramics as tissue engineering scaffolds for the repair of osteochondral defects: histological results, Acta Biomater. 9 (7) (2013) 7490–7505, https://doi.org/10.1016/j.actbio.2013.03.021.

[7] P. Nooeaid, V. Salih, J.P. Beier, A.R. Boccaccini, Osteochondral tissue engineering: scaffolds, stem cells and applications, J. Cell Mol. Med. 16 (10) (2012) 2247–2270, https://doi.org/10.1111/j.1582-4934.2012.01571.x.

[8] K.L. Moffat, I.N. Wang, S.A. Rodeo, H.H. Lu, Orthopedic interface tissue engineering for the biological fixation of soft tissue grafts, Clin. Sports Med. 28 (1) (2009) 157–176, https://doi.org/10.1016/j.csm.2008.08.006.

[9] H. Ryu, M.H. Seo, J.A. Rogers, Bioresorbable metals for biomedical applications: from mechanical components to electronic devices, Adv. Healthcare Mater. 10 (17) (2021), e2002236, https://doi.org/10.1002/adhm.202002236.

[10] P.B. Malafaya, R.L. Reis, Bilayered chitosan-based scaffolds for osteochondral tissue engineering: influence of hydroxyapatite on in vitro cytotoxicity and dynamic bioactivity studies in a specific double-chamber bioreactor, Acta Biomater. 5 (2) (2009) 644–660, https://doi.org/10.1016/j.actbio.2008.09.017.

[11] I. Schleicher, K.S. Lips, U. Sommer, I. Schappat, A.P. Martin, G. Szalay, S. Hartmann, R. Schnettler, Biphasic scaffolds for repair of deep osteochondral defects in a sheep model, J. Surg. Res. 183 (1) (2013) 184–192, https://doi.org/10.1016/j.jss.2012.11.036.

[12] S. Khorshidi, A. Karkhaneh, A review on gradient hydrogel/fiber scaffolds for osteochondral regeneration, J. Tissue Eng. Regen. Med. 12 (4) (2018) e1974–e1990, https://doi.org/10.1002/term.2628.

[13] L.P. Yan, J.M. Oliveira, A.L. Oliveira, R.L. Reis, Current concepts and challenges in osteochondral tissue engineering and regenerative medicine, ACS Biomater. Sci. Eng. 1 (4) (2015) 183–200, https://doi.org/10.1021/ab500038y.

[14] P.G. Alexander, R. Gottardi, H. Lin, T.P. Lozito, R.S. Tuan, Three-dimensional osteogenic and chondrogenic systems to model osteochondral physiology and degenerative joint diseases, Exp. Biol. Med. (Maywood, NJ, U. S.) 239 (9) (2014) 1080–1095, https://doi.org/10.1177/1535370214539232.

[15] T. Nie, L. Xue, M. Ge, H. Ma, J. Zhang, Fabrication of poly(L-lactic acid) tissue engineering scaffolds with precisely controlled gradient structure, Mater. Lett. 176 (2016) 25–28, https://doi.org/10.1016/j.matlet.2016.04.078.

[16] T. Yang, M. Tamaddon, L. Jiang, J. Wang, Z. Liu, Z. Liu, H. Meng, Y. Hu, J. Gao, X. Yang, Y. Zhao, Y. Wang, A. Wang, Q. Wu, C. Liu, J. Peng, X. Sun, Q. Xue, Bilayered scaffold with 3D printed stiff subchondral bony compartment to provide constant mechanical support for long-term cartilage regeneration, J Orthop Translat 30 (2021) 112–121, https://doi.org/10.1016/j.jot.2021.09.001.

[17] X. Duan, X. Zhu, X. Dong, J. Yang, F. Huang, S. Cen, F. Leung, H. Fan, Z. Xiang, Repair of large osteochondral defects in a beagle model with a novel type I collagen/glycosaminoglycan-porous titanium biphasic scaffold, Mater. Sci. Eng., C 33 (7) (2013) 3951–3957, https://doi.org/10.1016/j.msec.2013.05.040.

[18] X. Wei, B. Liu, G. Liu, F. Yang, F. Cao, X. Dou, W. Yu, B. Wang, G. Zheng, L. Cheng, Z. Ma, Y. Zhang, J. Yang, Z. Wang, J. Li, D. Cui, W. Wang, H. Xie, L. Li, F. Zhang, W. C. Lineaweaver, D. Zhao, Mesenchymal stem cell-loaded porous tantalum integrated with biomimetic 3D collagen-based scaffold to repair large osteochondral defects in goats, Stem Cell Res. Ther. 10 (1) (2019) 72, https://doi.org/10.1186/s13287-019-1176-2.

[19] R.W. McCalden, J.A. McGeough, C.M. Court-Brown, Age-related changes in the compressive strength of cancellous bone. The relative importance of changes in density and trabecular architecture, J Bone Joint Surg Am 79 (3) (1997) 421–427, https://doi.org/10.2106/00004623-199703000-00016.

[20] H.H. Xu, C.G. Simon Jr., Fast setting calcium phosphate-chitosan scaffold: mechanical properties and biocompatibility, Biomaterials 26 (12) (2005) 1337–1348, https://doi.org/10.1016/j.biomaterials.2004.04.043.

[21] H.F. Li, X.H. Xie, Y.F. Zheng, Y. Cong, F.Y. Zhou, K.J. Qiu, X. Wang, S.H. Chen, L. Huang, L. Tian, L. Qin, Development of biodegradable Zn-1X binary alloys with nutrient alloying elements Mg, Ca and Sr, Sci. Rep. 5 (2015), 10719, https://doi.org/10.1038/srep10719.

[22] G. Katarivas Levy, J. Goldman, E. Aghion, The prospects of zinc as a structural material for biodegradable implants—a review paper, Metals 7 (10) (2017) 402.

[23] J. Venezuela, M.S. Dargusch, The influence of alloying and fabrication techniques on the mechanical properties, biodegradability and biocompatibility of zinc: a comprehensive review, Acta Biomater. 87 (2019) 1–40, https://doi.org/10.1016/j.actbio.2019.01.035.

[24] J. Sun, X. Zhang, Z.Z. Shi, X.X. Gao, H.Y. Li, F.Y. Zhao, J.Q. Wang, L.N. Wang, Development of a high-strength Zn-Mn-Mg alloy for ligament reconstruction fixation, Acta Biomater. 119 (2021) 485–498, https://doi.org/10.1016/j.actbio.2020.10.032.

[25] M. Bobby Kannan, J. Chappell, H. Khakbaz, M. Taherishargh, T. Fiedler, Biodegradable 3D porous zinc alloy scaffold for bone fracture fixation devices, Adv. Funct. Mater. 3 (6) (2020), e10108, https://doi.org/10.1002/mds3.10108.
[26] P.K. Bowen, J. Drelich, J. Goldman, Zinc exhibits ideal physiological corrosion behavior for bioabsorbable stents, Adv. Mater. 25 (18) (2013) 2577–2582, https://doi.org/10.1002/adma.201300226.
[27] L. Liu, F. Yuan, M. Zhao, C. Gao, P. Feng, Y. Yang, S. Yang, C. Shuai, Rare earth element yttrium modified Mg-Al-Zn alloy: microstructure, degradation properties and hardness, Materials 10 (5) (2017), https://doi.org/10.3390/ma10050477.
[28] Y. Li, H. Jahr, K. Lietaert, P. Pavanram, A. Yilmaz, L.I. Fockaert, M.A. Leeflang, B. Pouran, Y. Gonzalez-Garcia, H. Weinans, J.M.C. Mol, J. Zhou, A.A. Zadpoor, Additively manufactured biodegradable porous iron, Acta Biomater. 77 (2018) 380–393, https://doi.org/10.1016/j.actbio.2018.07.011.
[29] Y. Li, J. Zhou, P. Pavanram, M.A. Leeflang, L.I. Fockaert, B. Pouran, N. Tümer, K. U. Schröder, J.M.C. Mol, H. Weinans, H. Jahr, A.A. Zadpoor, Additively manufactured biodegradable porous magnesium, Acta Biomater. 67 (2018) 378–392, https://doi.org/10.1016/j.actbio.2017.12.008.
[30] Y. Li, P. Pavanram, J. Zhou, K. Lietaert, P. Taheri, W. Li, H. San, M.A. Leeflang, J. M.C. Mol, H. Jahr, A.A. Zadpoor, Additively manufactured biodegradable porous zinc, Acta Biomater. 101 (2020) 609–623, https://doi.org/10.1016/j.actbio.2019.10.034.
[31] Y. Li, P. Pavanram, J. Zhou, K. Lietaert, P.F.S.L. Bobbert, Y. Kubo, M.A. Leeflang, H. Jahr, A.A. Zadpoor, Additively manufactured functionally graded biodegradable porous zinc, Biomater. Sci. 8 (9) (2020) 2404–2419, https://doi.org/10.1039/c9bm01904a.
[32] Y. Li, H. Jahr, J. Zhou, A.A. Zadpoor, Additively manufactured biodegradable porous metals, Acta Biomater. 115 (2020) 29–50, https://doi.org/10.1016/j.actbio.2020.08.018.
[33] Y. Li, W. Li, F.S.L. Bobbert, K. Lietaert, J.H. Dong, M.A. Leeflang, J. Zhou, A. A. Zadpoor, Corrosion fatigue behavior of additively manufactured biodegradable porous zinc, Acta Biomater. 106 (2020) 439–449, https://doi.org/10.1016/j.actbio.2020.02.001.
[34] A. Khader, T.L. Arinzeh, Biodegradable zinc oxide composite scaffolds promote osteochondral differentiation of mesenchymal stem cells, Adv. Funct. Mater. 117 (1) (2020) 194–209, https://doi.org/10.1002/bit.27173.
[35] L. Wang, X. Zhang, K. Yang, Y.V. Fu, T. Xu, S. Li, D. Zhang, L.-N. Wang, C.-S. Lee, A novel double-crosslinking-double-network design for injectable hydrogels with enhanced tissue adhesion and antibacterial capability for wound treatment, Adv. Funct. Mater. 30 (1) (2020), 1904156, https://doi.org/10.1002/adfm.201904156.
[36] L. Wang, K. Yang, X. Li, X. Zhang, D. Zhang, L.N. Wang, C.S. Lee, A double-crosslinked self-healing antibacterial hydrogel with enhanced mechanical performance for wound treatment, Acta Biomater. 124 (2021) 139–152, https://doi.org/10.1016/j.actbio.2021.01.038.
[37] B. Li, L. Wang, F. Xu, X. Gang, U. Demirci, D. Wei, Y. Li, Y. Feng, D. Jia, Y. Zhou, Hydrosoluble, UV-crosslinkable and injectable chitosan for patterned cell-laden microgel and rapid transdermal curing hydrogel in vivo, Acta Biomater. 22 (2015) 59–69, https://doi.org/10.1016/j.actbio.2015.04.026.
[38] X. Sun, Q. Lang, H. Zhang, L. Cheng, Y. Zhang, G. Pan, X. Zhao, H. Yang, Y. Zhang, H.A. Santos, W. Cui, Electrospun photocrosslinkable hydrogel fibrous scaffolds for rapid in vivo vascularized skin flap regeneration, Adv. Funct. Mater. 27 (2) (2017), 1604617, https://doi.org/10.1002/adfm.201604617.
[39] O.F. Restaino, R. Finamore, A. Stellavato, P. Diana, E. Bedini, M. Trifuoggi, M. De Rosa, C. Schiraldi, European chondroitin sulfate and glucosamine food supplements: a systematic quality and quantity assessment compared to pharmaceuticals, Carbohydr. Polym. 222 (2019), 114984, https://doi.org/10.1016/j.carbpol.2019.114984.
[40] X. Bai, S. Lü, Z. Cao, B. Ni, X. Wang, P. Ning, D. Ma, H. Wei, M. Liu, Dual crosslinked chondroitin sulfate injectable hydrogel formed via continuous Diels-Alder (DA) click chemistry for bone repair, Carbohydr. Polym. 166 (2017) 123–130, https://doi.org/10.1016/j.carbpol.2017.02.062.
[41] Y.S. Kim, E.H. Park, Y.C. Kim, Y.G. Koh, Clinical outcomes of mesenchymal stem cell injection with arthroscopic treatment in older patients with osteochondral lesions of the talus, Am. J. Sports Med. 41 (5) (2013) 1090–1099, https://doi.org/10.1177/0363546513479018.
[42] L.A. Fortier, J.U. Barker, E.J. Strauss, T.M. McCarrel, B.J. Cole, The role of growth factors in cartilage repair, Clin. Orthop. Relat. Res. 469 (10) (2011) 2706–2715, https://doi.org/10.1007/s11999-011-1857-3.
[43] F. David, T.J. Levingstone, W. Schneeweiss, M. de Swarte, H. Jahns, J.P. Gleeson, F.J. O'Brien, Enhanced bone healing using collagen-hydroxyapatite scaffold implantation in the treatment of a large multiloculated mandibular aneurysmal bone cyst in a thoroughbred filly, J. Tissue Eng. Regen. Med. 9 (10) (2015) 1193–1199, https://doi.org/10.1002/term.2006.
[44] A.M.J. Getgood, S.J. Kew, R. Brooks, H. Aberman, T. Simon, A.K. Lynn, N. Rushton, Evaluation of early-stage osteochondral defect repair using a biphasic scaffold based on a collagen-glycosaminoglycan biopolymer in a caprine model, Knee 19 (4) (2012) 422–430, https://doi.org/10.1016/j.knee.2011.03.011.
[45] I. Calejo, R. Costa-Almeida, R.L. Reis, M.E. Gomes, A physiology-inspired multifactorial toolbox in soft-to-hard musculoskeletal interface tissue engineering, Trends Biotechnol. 38 (1) (2020) 83–98, https://doi.org/10.1016/j.tibtech.2019.06.003.
[46] W. Dai, L. Zhang, Y. Yu, W. Yan, F. Zhao, Y. Fan, C. Cao, Q. Cai, X. Hu, Y. Ao, 3D bioprinting of heterogeneous constructs providing tissue-specific microenvironment based on host–guest modulated dynamic hydrogel bioink for osteochondral regeneration, Adv. Funct. Mater. 32 (23) (2022), 2200710, https://doi.org/10.1002/adfm.202200710.
[47] D. Yin, H. Wu, C. Liu, J. Zhang, T. Zhou, J. Wu, Y. Wan, Fabrication of composition-graded collagen/chitosan–polylactide scaffolds with gradient architecture and properties, React. Funct. Polym. 83 (2014) 98–106, https://doi.org/10.1016/j.reactfunctpolym.2014.07.017.
[48] T.Z. Li, C.Z. Jin, B.H. Choi, M.S. Kim, Y.J. Kim, S.R. Park, J.H. Yoon, B.-H. Min, Using cartilage extracellular matrix (CECM) membrane to enhance the reparability of the bone marrow stimulation technique for articular cartilage defect in canine, Model 22 (20) (2012) 4292–4300, https://doi.org/10.1002/adfm.201102695.
[49] I. Martin, S. Miot, A. Barbero, M. Jakob, D. Wendt, Osteochondral tissue engineering, J. Biomech. 40 (4) (2007) 750–765.
[50] J. Hernigou, P. Verdonk, Y. Homma, R. Verdonk, S.B. Goodman, P. Hernigou, Nonoperative and operative bone and cartilage regeneration and orthopaedic biologics of the hip: an orthoregeneration network (ON) foundation hip review, Arthroscopy 38 (2) (2022) 643–656, https://doi.org/10.1016/j.arthro.2021.08.032.
[51] B. Sharma, S. Fermanian, M. Gibson, S. Unterman, D.A. Herzka, B. Cascio, J. Coburn, A.Y. Hui, N. Marcus, G.E. Gold, J.H. Elisseeff, Human cartilage repair with a photoreactive adhesive-hydrogel composite, Sci. Transl. Med. 5 (167) (2013) 167ra6, https://doi.org/10.1126/scitranslmed.3004838.
[52] R. Scaffaro, F. Lopresti, L. Botta, S. Rigogliuso, G. Ghersi, Integration of PCL and PLA in a monolithic porous scaffold for interface tissue engineering, J. Mech. Behav. Biomed. Mater. 63 (2016) 303–313, https://doi.org/10.1016/j.jmbbm.2016.06.021.
[53] R. Longley, A.M. Ferreira, P. Gentile, Recent approaches to the manufacturing of biomimetic multi-phasic scaffolds for osteochondral regeneration, Int. J. Mol. Sci. 19 (6) (2018), https://doi.org/10.3390/ijms19061755.
[54] N. Aslan, B. Aksakal, F. Findik, Fabrication of porous-Ti6Al4V alloy by using hot pressing technique and Mg space holder for hard-tissue biomedical applications, J. Mater. Sci. Mater. Med. 32 (7) (2021) 80, https://doi.org/10.1007/s10856-021-06546-2.
[55] M.S. Patel, J.R. McCormick, A. Ghasem, S.R. Huntley, J.P. Gjolaj, Tantalum: the next biomaterial in spine surgery? J Spine Surg 6 (1) (2020) 72–86, https://doi.org/10.21037/jss.2020.01.01.
[56] G. Li, H. Yang, Y. Zheng, X.H. Chen, J.A. Yang, D. Zhu, L. Ruan, K. Takashima, Challenges in the use of zinc and its alloys as biodegradable metals: perspective from biomechanical compatibility, Acta Biomater. 97 (2019) 23–45, https://doi.org/10.1016/j.actbio.2019.07.038.
[57] D. Zhu, I. Cockerill, Y. Su, Z. Zhang, J. Fu, K.W. Lee, J. Ma, C. Okpokwasili, L. Tang, Y. Zheng, Y.X. Qin, Y. Wang, Mechanical strength, biodegradation, and in vitro and in vivo biocompatibility of Zn biomaterials, ACS Appl. Mater. Interfaces 11 (7) (2019) 6809–6819, https://doi.org/10.1021/acsami.8b20634.
[58] H. Yang, B. Jia, Z. Zhang, X. Qu, G. Li, W. Lin, D. Zhu, K. Dai, Y. Zheng, Alloying design of biodegradable zinc as promising bone implants for load-bearing applications, Nat. Commun. 11 (1) (2020) 401, https://doi.org/10.1038/s41467-019-14153-7.
[59] W. Ding, Opportunities and challenges for the biodegradable magnesium alloys as next-generation biomaterials, Regen Biomater 3 (2) (2016) 79–86, https://doi.org/10.1093/rb/rbw003.
[60] Z. Zhang, B. Jia, H. Yang, Y. Han, Q. Wu, K. Dai, Y. Zheng, Zn0.8Li0.1Sr-a biodegradable metal with high mechanical strength comparable to pure Ti for the treatment of osteoporotic bone fractures: in vitro and in vivo studies, Biomaterials 275 (2021), 120905, https://doi.org/10.1016/j.biomaterials.2021.120905.
[61] L.-P. Yan, J.M. Oliveira, A.L. Oliveira, R.L. Reis, Current concepts and challenges in osteochondral tissue engineering and regenerative medicine, ACS Biomater. Sci. Eng. 1 (4) (2015) 183–200, https://doi.org/10.1021/ab500038y.
[62] R. Scaffaro, F. Lopresti, L. Botta, S. Rigogliuso, G. Ghersi, Integration of PCL and PLA in a monolithic porous scaffold for interface tissue engineering, J. Mech. Behav. Biomed. Mater. 63 (2016) 303–313, https://doi.org/10.1016/j.jmbbm.2016.06.021.
[63] S. Khorshidi, A. Karkhaneh, A review on gradient hydrogel/fiber scaffolds for osteochondral regeneration, J. Tissue Eng. Regen. Med. 12 (4) (2018) e1974–e1990, https://doi.org/10.1002/term.2628.
[64] D. Xia, Y. Qin, H. Guo, P. Wen, H. Lin, M. Voshage, J.H. Schleifenbaum, Y. Cheng, Y. Zheng, Additively manufactured pure zinc porous scaffolds for critical-sized bone defects of rabbit femur, Bioact. Mater. 19 (2023) 12–23, https://doi.org/10.1016/j.bioactmat.2022.03.010.
[65] D. Zhao, K. Yu, T. Sun, X. Jing, Y. Wan, K. Chen, H. Gao, Y. Wang, L. Chen, X. Guo, Q. Wei, Material–structure–function integrated additive manufacturing of degradable metallic bone implants for load-bearing applications, Adv. Funct. Mater. 33 (16) (2023), 2213128, https://doi.org/10.1002/adfm.202213128.
[66] J. Wang, F. Witte, T. Xi, Y. Zheng, K. Yang, Y. Yang, D. Zhao, J. Meng, Y. Li, W. Li, K. Chan, L. Qin, Recommendation for modifying current cytotoxicity testing standards for biodegradable magnesium-based materials, Acta Biomater. 21 (2015) 237–249, https://doi.org/10.1016/j.actbio.2015.04.011.
[67] A. Cerovic, I. Miletic, S. Sobajic, D. Blagojevic, M. Radusinovic, A. El-Sohemy, Effects of zinc on the mineralization of bone nodules from human osteoblast-like cells, Biol. Trace Elem. Res. 116 (1) (2007) 61–71, https://doi.org/10.1007/bf02685919.
[68] D. Zhu, Y. Su, M.L. Young, J. Ma, Y. Zheng, L. Tang, Biological responses and mechanisms of human bone marrow mesenchymal stem cells to Zn and Mg

biomaterials, ACS Appl. Mater. Interfaces 9 (33) (2017) 27453–27461, https://doi.org/10.1021/acsami.7b06654.
[69] X. Gao, Y. Xue, Z. Zhu, J. Chen, Y. Liu, X. Cheng, X. Zhang, J. Wang, X. Pei, Q. Wan, Nanoscale zeolitic imidazolate framework-8 activator of canonical MAPK signaling for bone repair, ACS Appl. Mater. Interfaces 13 (1) (2021) 97–111, https://doi.org/10.1021/acsami.0c15945.
[70] Y. Yu, G. Jin, Y. Xue, D. Wang, X. Liu, J. Sun, Multifunctions of dual Zn/Mg ion co-implanted titanium on osteogenesis, angiogenesis and bacteria inhibition for dental implants, Acta Biomater. 49 (2017) 590–603, https://doi.org/10.1016/j.actbio.2016.11.067.